Journal of Inflammation Research

Dovepress
Taylor & Francis Group

Open Access Full Text Article

ORIGINAL RESEARCH

Cross-Disease Identification of FBP1 in Atherosclerosis and Calcific Aortic Valve Disease via Integrated Bioinformatics and Validation: Functional Analysis and Therapeutic Target Exploration

Haowen Xu[1,*], Yifan Xu[2,*], Xueyi Wang[3], Zhisheng Yan[4], Ting Geng[5], Jinpeng Wu[2], Yongxin Li[1], Mingjin Guo[1]

[1]Department of Vascular Surgery, The Affiliated Hospital of Qingdao University, Qingdao, 266000, People's Republic of China; [2]Department of Neurosurgery, The Affiliated Hospital of Qingdao University, Qingdao, 266000, People's Republic of China; [3]Department of Vascular Surgery, Rongcheng City People's Hospital, Rongcheng, 264300, People's Republic of China; [4]Department of Interventional Medicine, The Eighth People's Hospital of Qingdao, Qingdao, 266000, People's Republic of China; [5]Interventional Operating Room, The Eighth People's Hospital of Qingdao, Qingdao, 266000, People's Republic of China

*These authors contributed equally to this work

Correspondence: Mingjin Guo; Yongxin Li, Department of Vascular Surgery, The Affiliated Hospital of Qingdao University, 16 Jiang Su Road, Qingdao, 266000, People's Republic of China, Email qduahvasc@163.com; Li.yongxin@outlook.com

Purpose: Atherosclerosis (AS) and calcific aortic valve disease (CAVD) are common in aging populations and share metabolic dysregulation, chronic inflammation, and cellular aging. Shared immunometabolic biomarkers and therapeutic targets remain insufficiently defined. This study aimed to identify Cross-disease biomarkers linking AS and CAVD and to explore their translational potential.

Methods: Four Gene Expression Omnibus (GEO) microarray datasets related to AS and CAVD were integrated. Differentially expressed genes (DEGs) were identified within each disease, and Cross-disease genes (CGs) were obtained by intersecting DEGs across the two diseases. Functional enrichment and protein–protein interaction analyses were performed. Machine learning (LASSO and Random Forest) refined candidate biomarkers. Immune infiltration was estimated with CIBERSORT, and a microRNA–transcription factor regulatory network was constructed. Molecular docking screened small molecules targeting the hub gene. Diagnostic performance was evaluated in independent datasets, and expression was validated in human tissues by qPCR and Western blot.

Results: We identified 147 CGs enriched in immune and metabolic pathways. Fructose-1,6-bisphosphatase 1 (FBP1) emerged as a hub gene with strong diagnostic value across datasets. FBP1 expression correlated with alterations in multiple immune cell populations and was embedded within a regulatory network of predicted microRNAs and transcription factors. Docking analysis highlighted apigenin and kaempferol as candidate FBP1-targeting compounds. Experimental validation confirmed FBP1 upregulation in AS and CAVD tissues.

Discussion: FBP1 represents a shared immunometabolic biomarker and potential therapeutic target that links metabolic reprogramming to immune dysregulation in AS and CAVD. These findings provide a rationale for further translational studies evaluating FBP1-centered interventions.

Keywords: atherosclerosis, calcific aortic valve disease, machine learning, immunology, molecular docking

Introduction

Degenerative vascular diseases are increasingly prevalent with population aging and lifestyle shifts.[1,2] Atherosclerosis (AS) and calcific aortic valve disease (CAVD) are major contributors to the cardiovascular burden in older adults.[3,4] In 2019, cardiovascular diseases, primarily driven by atherosclerosis, affected approximately 523 million individuals worldwide.[3] Concurrently, CAVD has emerged as the most common valvular heart disease in older adults, with severe aortic valve stenosis affecting approximately 12% of individuals aged 75 years or older and resulting in over 100,000 annual deaths globally.[5] Both

Received: 15 May 2025
Accepted: 12 November 2025
Published: 19 November 2025

conditions typically progress silently until advanced stages, eventually causing serious complications such as myocardial infarction, heart failure, and significantly reduced quality of life.[6]

Previously considered passive consequences of aging,[7,8] recent studies indicate that both AS and CAVD involve active cellular processes, sharing critical pathological mechanisms including metabolic dysregulation,[9,10] immune-mediated inflammation,[11,12] and extracellular matrix (ECM) remodeling.[13,14] Lipid accumulation and oxidation drive oxidative stress, endothelial injury, and immune-cell recruitment.[15,16] Metabolic abnormalities, notably enhanced glycolysis and altered lipid metabolism, drive plaque formation in AS and promote valve calcification in CAVD.[17,18] In arterial lesions, vascular smooth muscle cells (VSMCs) undergo phenotypic switching from a contractile state to synthetic, macrophage-like, and osteogenic-like phenotypes, thereby accelerating ECM remodeling, modulating lipid/inflammatory responses, and promoting microcalcification.[19] In valvular tissue, valvular interstitial cells (VICs) acquire myofibroblastic and osteogenic programs that couple to immunometabolic cues and drive leaflet fibrosis and calcification.[17] These common mechanisms suggest shared molecular targets, presenting opportunities for unified prevention and treatment strategies.[20]

To address the unmet need for effective diagnostics and therapies, this study systematically identified 147 CGs commonly dysregulated in both AS and CAVD. Among these, FBP1 was highlighted as a metabolism-related hub gene through machine learning, exhibiting robust diagnostic performance across multiple independent datasets. Immune infiltration analysis revealed disease-specific associations between FBP1 expression and immune cell composition. Regulatory analysis suggested upstream miRNAs and transcription factors potentially regulating FBP1. Molecular docking predicted strong binding affinities between FBP1 and candidate therapeutic compounds, including apigenin and kaempferol. Experimental validation further supported FBP1 overexpression in clinical AS and CAVD tissues. Collectively, these findings offer new perspectives on shared pathogenic mechanisms and highlight FBP1 as a potential biomarker and therapeutic target. A schematic overview of the integrative analysis is shown in Figure 1.

Materials and Methods

Microarray Data Collection and Processing

Four datasets related to AS and CAVD (GSE100927, GSE43292, GSE12644, and GSE83453) were retrieved from the GEO database (https://www.ncbi.nlm.nih.gov/geo/).[21] Details are provided in Supplementary Table 1. GSE100927 (AS) and GSE12644 (CAVD) served as discovery datasets, while GSE43292 (AS) and GSE83453 (CAVD) were used for validation. Expression data were normalized using normalizeBetweenArrays in R. A total of 1468 metabolism-related genes were obtained from GeneCards (https://www.genecards.org/),[22] selecting only protein-coding genes with relevance scores >2. Batch effects within datasets were corrected using quantile normalization, and PCA was conducted using the "FactoMineR" and "factoextra" packages.

Analysis of Differentially Expressed Genes (DEGs)

Bioinformatic preprocessing of CAVD and AS datasets consisted of background signal correction, quantile normalization (performed using the R package "preprocessCore"), and gene symbol standardization. Differentially expressed genes (DEGs) were identified via the "limma" package,[23] applying consistent thresholds ($|\log2 \text{ fold change (log2FC)}| \geq 0.5$, $p < 0.05$) across both datasets. Genes were categorized as upregulated ($\log2FC \geq 0.5$) or downregulated ($\log2FC \leq -0.5$); non-significant genes were excluded. DEGs were visualized using volcano plots generated with ggplot2, and the final gene lists were archived for subsequent functional analyses.

Identification of Cross-Disease Genes(CGs)

The CGs were identified by comparing DEGs between the AS and CAVD datasets. Initially, gene lists for upregulated and downregulated DEGs were separately extracted from each dataset. Subsequently, overlapping upregulated and downregulated genes common to both diseases were identified using the intersect function in R.

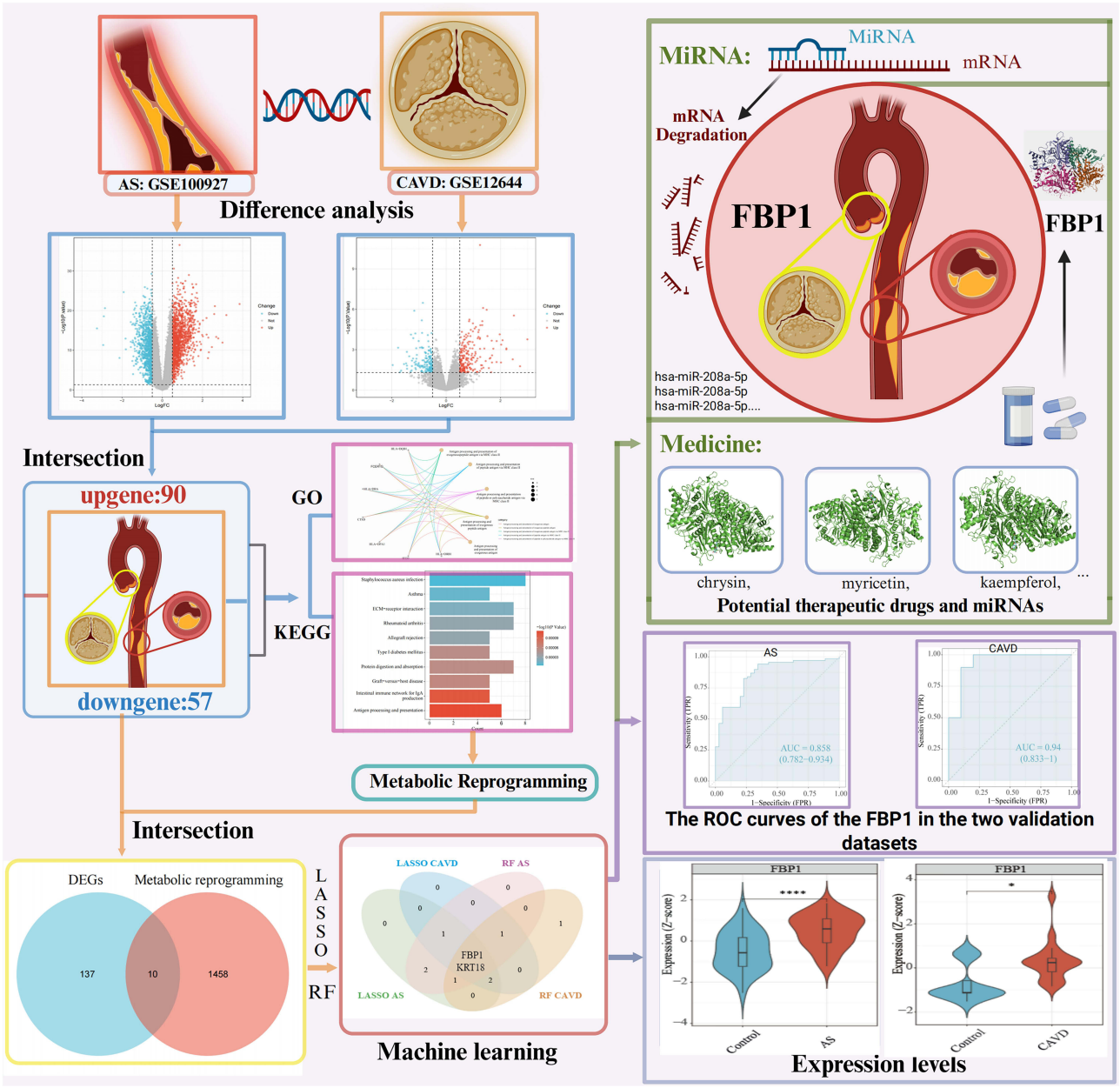

Figure 1 Overall design of the study. Significance: P < 0.05 (*), P < 0.0001 (****).

Functional Enrichment, Pathway, and Correlation Analyses

Functional enrichment of hub genes was conducted using GO and KEGG analyses.[24,25] Gene symbols were converted to Entrez IDs via the bitr function in the "clusterProfiler" package.[26] Enrichment was performed with thresholds of $p < 0.05$ and $q < 0.1$, and the top 10 terms were visualized using dot, bar, and network plots. FBP1 expression data were extracted and grouped by upper and lower quartiles. Differential analysis was conducted using "limma", with p-values adjusted by the Benjamini-Hochberg method. Gene set enrichment analysis (GSEA) was performed on ranked log fold changes using KEGG gene sets,[27] and significant pathways (adjusted $p < 0.05$) were visualized with gseaplot2 and patchwork. For correlation analysis, gene-expression matrices from two independent cohorts were quantile-normalized (preprocessCore) and duplicate symbols collapsed (limma); Spearman's rank correlations were then computed between a prespecified target and phenotype marker panels, with two-sided nominal significance set at $P < 0.05$.

https://doi.org/10.2147/JIR.S540540

Machine Learning-Based Hub Genes Refinement

To identify candidate genes for CGs, two machine learning approaches were applied: LASSO logistic regression using the "glmnet" package,[28] and the random forest algorithm via the "randomForest" package.[29] For LASSO, predictors were standardized internally and 10-fold cross-validation was used to select λ at lambda.min; genes with non-zero coefficients at this λ were retained. For random forest, models were fit with ntree = 1000, default mtry = $\lfloor\sqrt{p}\rfloor$ for classification, importance = TRUE, and proximity = TRUE; variables were ranked by MeanDecreaseGini, and the top 7 features were retained. A fixed seed (set.seed(2024)) ensured reproducibility. The intersection of genes selected by both methods was used to determine the final set of candidate biomarkers.

Construction of a Diagnostic Model

Four GEO datasets were employed to construct a predictive model based on hub-gene expression. Receiver-operating-characteristic (ROC) analysis was conducted with the "pROC" package,[30] using the area under the curve (AUC) as the principal measure of discriminative performance. Model calibration was evaluated with bootstrap-derived calibration curves, and clinical utility was assessed through decision-curve analysis (DCA). Finally, a nomogram that integrates hub-gene expression with relevant clinical variables was generated using the "rms" package.

Immune Microenvironment Characterization

CIBERSORT was applied to estimate the relative abundance of 22 immune-cell subsets in the AS and CAVD datasets,[28] using the LM22 signature matrix. Cell-type proportions between disease and control groups were compared with the Wilcoxon rank-sum test, and Spearman rank-correlation analysis was used to examine associations between hub-gene expression and immune-cell fractions. Immune-infiltration patterns were visualised with the "ggplot2" package, and statistical significance was set at $p < 0.05$.

Regulatory Network of Hub Gene

The hub gene was first localised to its chromosomal band, establishing a cytogenetic reference for subsequent analyses. A protein–protein-interaction network centred on gene was then constructed with STRING.[31] Candidate microRNAs were screened in miRWalk under stringent thermodynamic and conservation criteria (free energy < –20 kcal mol^{-1}, AU content > 0.40, perfect seed match, PhyloP stem and flank scores > 0.50, ≥ 15 matched nucleotides, binding region ≥ 15 nt, and longest consecutive pairing ≥ 10 nt).[32] The regulatory effects of these microRNAs on gene expression were evaluated in downstream analyses. Transcription factors were predicted by integrating results from the ENCODE, hTFtarget and KnockTF databases,[33] generating a unified TF–miRNA–gene regulatory network. All interactions were merged and visualised in Cytoscape to provide an intuitive representation of the multilayer regulatory landscape surrounding the target gene.

Drug Prediction and Docking

Drug–gene interactions were queried in DSigDB,[34] and the corresponding small-molecule structures were downloaded from PubChem. Blind molecular docking was then conducted with CB-Dock2;[35] the pose exhibiting the lowest AutoDock Vina score (kcal/mol) was retained for further evaluation. Two-dimensional interaction maps were generated in Discovery Studio, and PyMOL was used to render three-dimensional complexes, providing a detailed depiction of ligand–protein contacts.

Patients and Samples

This study was approved by the Institutional Review Board of The Affiliated Hospital of Qingdao University (QYFY WZLL 29793) and conducted in accordance with the Declaration of Helsinki. Written informed consent was obtained from all surgical participants, including five patients with common carotid artery stenosis who each provided paired carotid specimens (advanced atherosclerotic intima and plaque-adjacent, less-affected intima) during endarterectomy, as well as patients undergoing lower-extremity amputation or aortic valve replacement. Control vascular and valvular tissues were obtained post-mortem under institutional authorization from individuals who died suddenly of accidental

causes; in all such cases, legal next-of-kin provided consent for body donation, and baseline information for deceased donors was supplied by their relatives. All samples were de-identified at the source, snap-frozen in liquid nitrogen immediately after excision, and stored at −80 °C until analysis. Specimen arterial type and comorbidities (eg, hypertension, diabetes, smoking status) for each sample are summarized in Supplementary Excel 1.

HE and Oil Red O Staining

For HE, tissues were fixed in 10% neutral-buffered formalin, paraffin-embedded, and sectioned at 4 μm. Slides were deparaffinized, rehydrated, stained with hematoxylin and eosin by standard protocols, dehydrated, cleared, and coverslipped. For Oil Red O (ORO), adjacent specimens were processed as frozen tissue: embedded in OCT, snap-frozen, cryosectioned at 8–10 μm, equilibrated to room temperature, briefly fixed, stained with ORO working solution from isopropanol stock, differentiated in 60% isopropanol, counterstained with hematoxylin, and mounted with aqueous medium. Images were acquired under identical exposure settings; scale bars: low-magnification 2.5 mm, high-magnification 250 μm.

Western Blot

Total protein was quantified with a BCA kit (Elabscience, China) after ultrasonic lysis. Equal aliquots were denatured, resolved by SDS-PAGE, and transferred to PVDF membranes. After blocking, membranes were incubated overnight (1:2000, Proteintech, cat. 12842-1-AP), washed with TBST, and exposed to HRP-conjugated secondary antibody for 2 h. Signal was developed by enhanced chemiluminescence (Vazyme) and band intensity was quantified with Image J.[36]

Quantitative Real-Time PCR

Total RNA was extracted with TRIzol (Thermo Fisher) and quantified by NanoDrop (A260/280 ≥ 1.8). One microgram was reverse-transcribed using the PrimeScript RT kit (Takara). qPCR was performed on a Bio-Rad CFX Opus with SYBR-Green premix (TsingKe) under the following programme: 95 °C × 30s, then 40 cycles of 95 °C × 5s and 60 °C × 15s, followed by a melting-curve step. Primer sequences were: FBP1 gene forward 5′-CGCGCACCTCTATGGCATT-3′ and reverse 5′-TTCTTCTGACACGAGAACACAC-3′. Relative expression was calculated by the $2^{-\Delta\Delta Ct}$ method, and group differences were assessed with an independent-samples *t*-test ($p < 0.05$), Ct values were normalized to GAPDH.

Statistical Analysis and Data Visualization

All analyses were conducted in R 4.3.1. Group differences were assessed with two-sided Wilcoxon tests, and variable associations with Spearman correlation; $p < 0.05$ was considered significant.

Results

Identification of Differentially Expressed Genes (DEGs) in AS and CAVD

Initially, we normalized the AS and CAVD gene-expression datasets (Supplementary Figure 1). Differential expression analysis identified 2290 significant DEGs in the AS dataset (1297 upregulated, 993 downregulated) and 373 in the CAVD dataset (213 upregulated, 160 downregulated) (Figure 2A and B). Hierarchical clustering of the 50 most variable transcripts robustly separated disease from control samples in both datasets (Figure 2C and D). Intersection analysis yielded 147 consensus DEGs shared by AS and CAVD 90 upregulated and 57 downregulated (Figure 2E and F). Detailed up-down-regulation genes can be found in Supplementary Table 2.

Functional enrichment profiling delineated distinct pathogenic programmes (Supplementary Figure 2). In AS, DEGs were chiefly associated with cytokine production and leukocyte migration and were over-represented in KEGG pathways such as rheumatoid arthritis and lysosome. In contrast, CAVD-specific DEGs were largely involved in extracellular-matrix organisation and collagen fibril assembly, enriching principally the ECM–receptor interaction and focal-adhesion pathways (Supplementary Figure 2A–D).

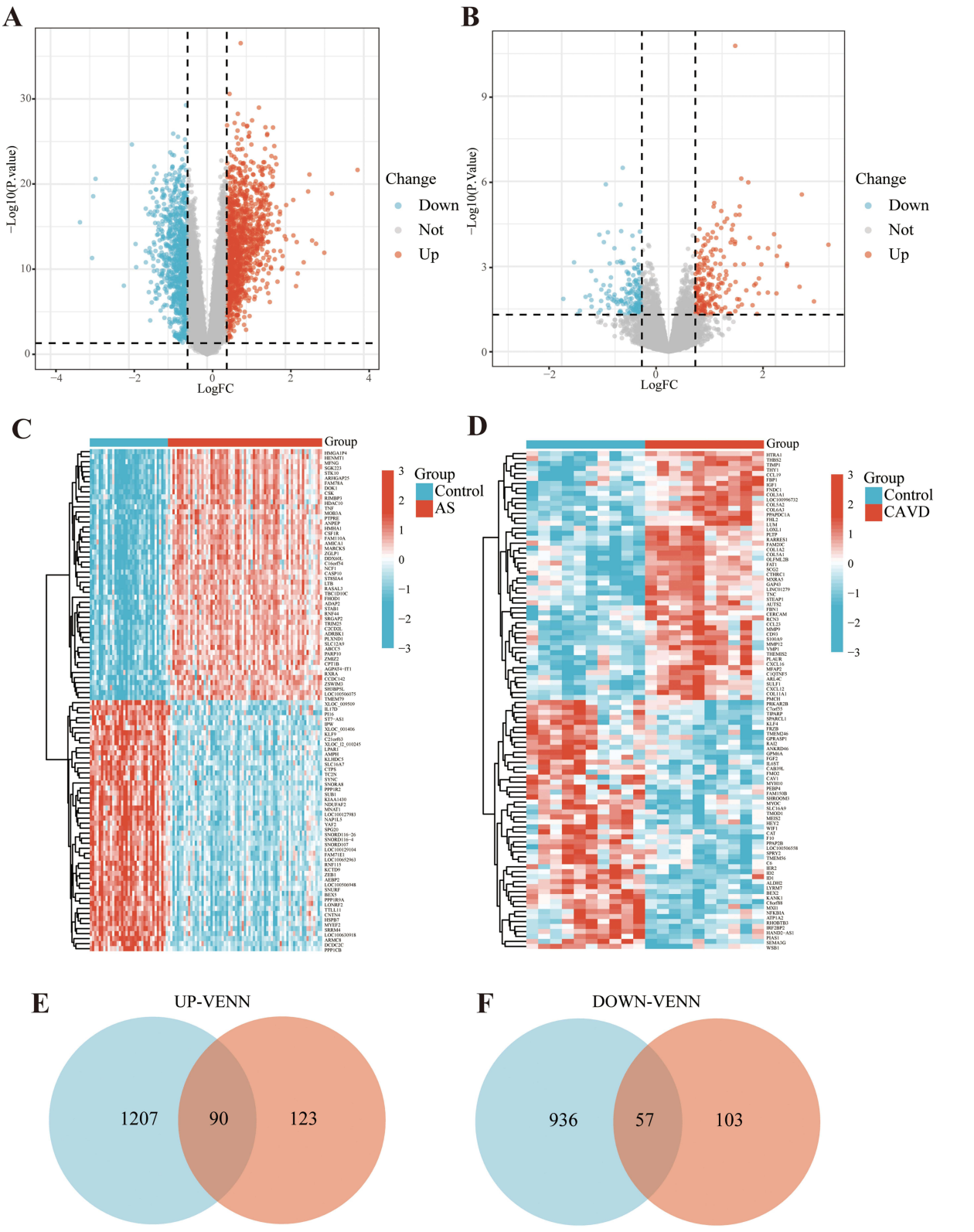

Figure 2 Cross-disease genes expression analysis. (**A** and **B**) Volcano plots of DEGs in AS and CAVD. (**C** and **D**) Heatmaps illustrate the expression patterns of corresponding DEGs in AS and CAVD. (**E** and **F**) Venn diagram illustrates the intersection analysis of CGs in AS and CAVD.

Functional Characterization of Overlapping DEGs

Analysis of the 147 consensus DEGs identified in both AS and CAVD revealed pronounced enrichment in immune-regulatory and Metabolic processes. The GO profiling indicated significant over-representation of antigen processing and presentation via MHC class II, together with pathways linked to ECM organisation (Figure 3A). The KEGG analysis

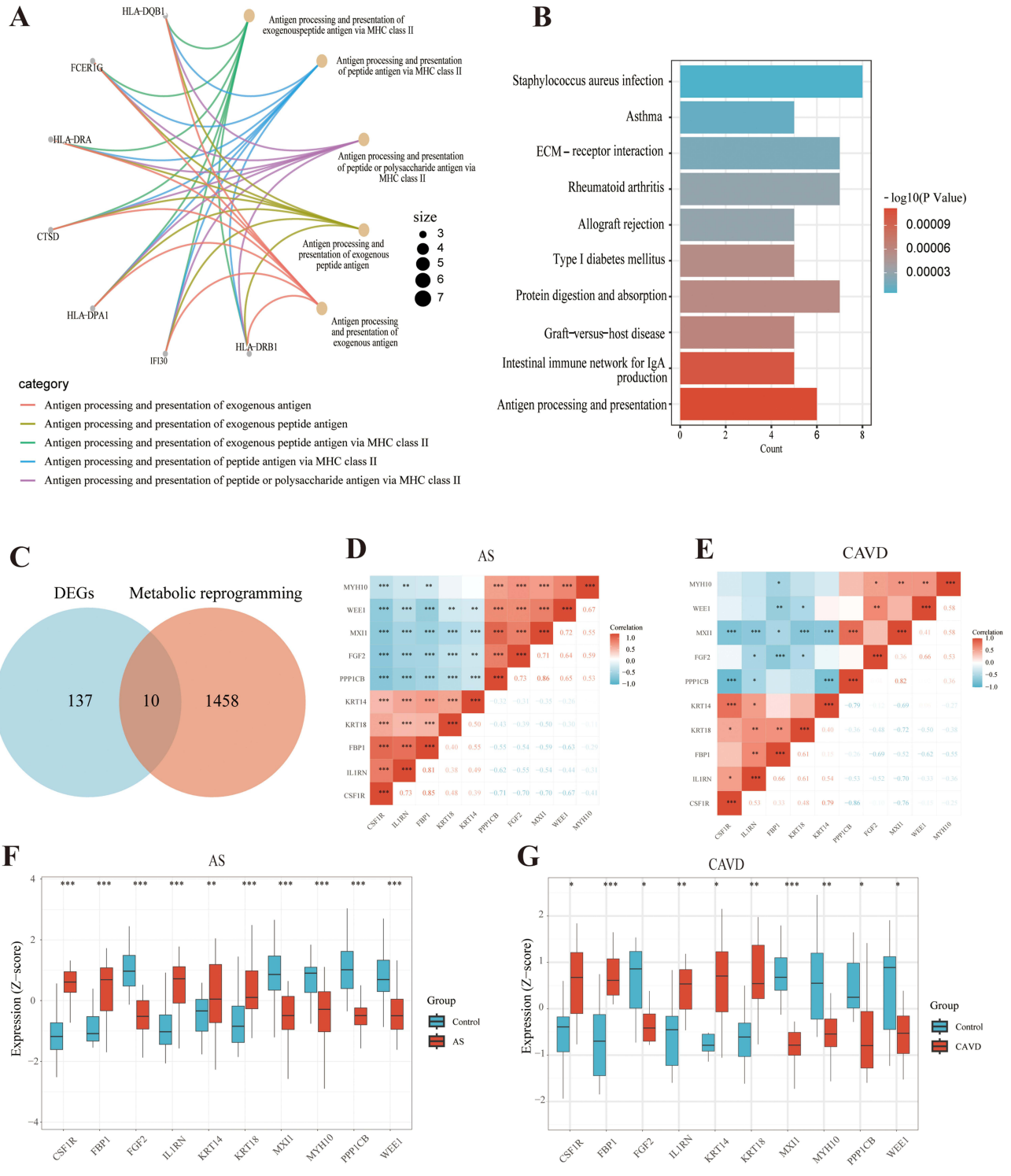

Figure 3 Integrated analysis of CGs and identification of metabolism-related CGs. (**A** and **B**) GO and KEGG enrichment analyses of 147 consensus CGs in AS and CAVD. (**C**) Venn diagram showing the intersection between shared DEGs and metabolism-related genes, identifying 10 overlapping candidates. (**D** and **E**) Co-expression correlations of the 10 hub genes in AS and CAVD datasets. (**F** and **G**) Expression levels of the 10 hub genes in AS and CAVD datasets. Significance: P < 0.05 (*), P < 0.01 (**), P < 0.001 (***).

https://doi.org/10.2147/JIR.S540540

further highlighted convergence in lysosomal signalling and ECM-receptor interaction, implying shared metabolism-related alterations between the two diseases (Figure 3B). Network interrogation pointed to close interplay among immune mediators and ECM components, suggesting a coordinated relationship among metabolic reprogramming, immune activation and structural remodelling in vascular pathology.

Intersecting these 147 DEGs with a curated list of 1468 metabolism-related genes yielded ten overlapping candidate genes: CSF1R, IL1RN, FBP1, KRT18, KRT14, PPP1CB, FGF2, MXI1, WEE1 and MYH10 (Figure 3C). Correlation analysis within the AS dataset demonstrated strong positive associations between FBP1 and KRT14, KRT18, IL1RN and CSF1R (Figure 3D), whereas these correlations were comparatively weaker in CAVD (Figure 3E). All ten genes displayed significant differential expression in both AS and CAVD datasets (Figure 3F and G). Collectively, the data delineate a common regulatory axis that integrates metabolic, immune and ECM-related signals, potentially underlying the pathogenesis of vascular calcification.

Machine Learning-Based Biomarker Identification

To delineate candidate biomarkers for AS and CAVD, we applied LASSO regression and RF modelling to the respective transcriptomic datasets. In the AS dataset, LASSO retained eight informative genes-CSF1R, IL1RN, FBP1, KRT14, KRT18, PPP1CB, FGF2 and MYH10 (Figure 4A and B). RF ranking likewise prioritised PPP1CB, CSF1R, FGF2, MXI1, FBP1, KRT18 and IL1RN (Figure 4C and D).

In the CAVD dataset, LASSO selected six candidates: FBP1, KRT18, KRT14, FGF2, MXI1 and MYH10 (Figure 4E and F). RF algorithm, in turn, highlighted MXI1, FBP1, KRT18, WEE1, PPP1CB, KRT14 and MYH10 (Figure 4G and H). Intersection of the LASSO and RF outputs across both diseases identified FBP1 and KRT18 as CGs (Figure 5A), implicating these genes as potential common drivers of AS and CAVD.

Developing a Disease Risk Model Using Diagnostic Biomarkers

To verify the expression profiles of the two candidate genes, four independent datasets were interrogated. Only FBP1 displayed uniformly elevated transcript levels across all datasets (Figure 5B–E). Receiver-operating-characteristic analysis confirmed robust discrimination in each dataset, with area-under-the-curve values exceeding 0.70 (Figure 6A–D). Calibration plots demonstrated close concordance between predicted and observed outcomes, as bias-corrected lines nearly overlapped the ideal diagonal (Figure 6E–H). Decision-curve analysis indicated a clear net clinical benefit for the FBP1-based model within the 0.20–0.80 probability range, surpassing both "treat-all" and "treat-none" strategies (Figure 6I–L). A nomogram integrating FBP1 expression with key clinical variables offers a practical tool for individual risk estimation, and schematic diagrams illustrate the structure of the AS and CAVD prediction models centred on FBP1 (Figure 6M and N). Collectively, these findings confirm elevated FBP1 expression and substantiate its strong predictive performance in both disorders.

Immune Microenvironment Characterization

Immune-cell infiltration was assessed with CIBERSORT in AS and CAVD tissues and their respective controls. Heatmaps and box-and-whisker plots summarised the relative abundance of 22 leukocyte subsets (Figure 7A and B). Compared with controls, AS specimens displayed higher proportions of memory B cells, M0 macrophages, γδ T cells and activated mast cells, alongside lower proportions of naïve B cells, plasma cells, resting CD4-memory T cells, activated natural-killer cells and monocytes (Figure 7C). CAVD specimens exhibited a parallel increase in M0 macrophages and γδ T cells and a corresponding decrease in activated natural-killer cells and monocytes (Figure 7D).

Correlation analysis showed that, in AS, FBP1 expression correlated negatively with resting CD4-memory T cells, M1 macrophages, monocytes and activated natural-killer cells, and positively with M0 macrophages, γδ T cells and activated mast cells (Figure 7E). In CAVD, FBP1 was negatively associated with monocytes, activated natural-killer cells and M2 macrophages, and positively associated with activated mast cells (Figure 7F). These findings indicate that FBP1 is closely linked to the immune microenvironment in both disorders and may participate in a shared immunoregulatory mechanism underlying atherosclerosis and calcific aortic-valve disease.

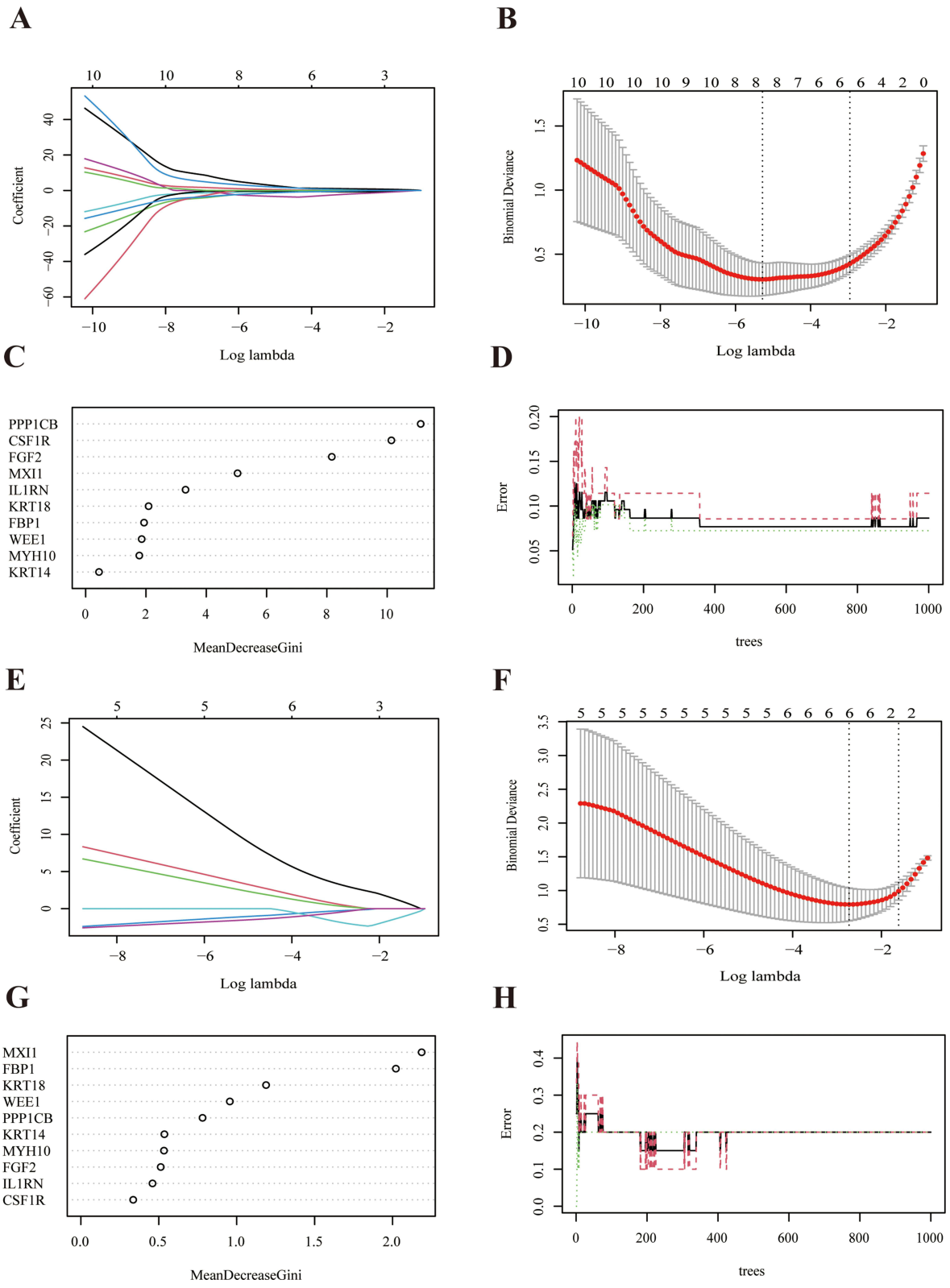

Figure 4 Identification of hub genes in AS and CAVD by machine learning. (**A** and **B**) LASSO regression analysis in the AS dataset. (**C** and **D**) Random forest (RF) analysis in the AS dataset. (**E** and **F**) LASSO regression in the CAVD dataset. (**G** and **H**) RF analysis in the CAVD dataset.

https://doi.org/10.2147/JIR.S540540

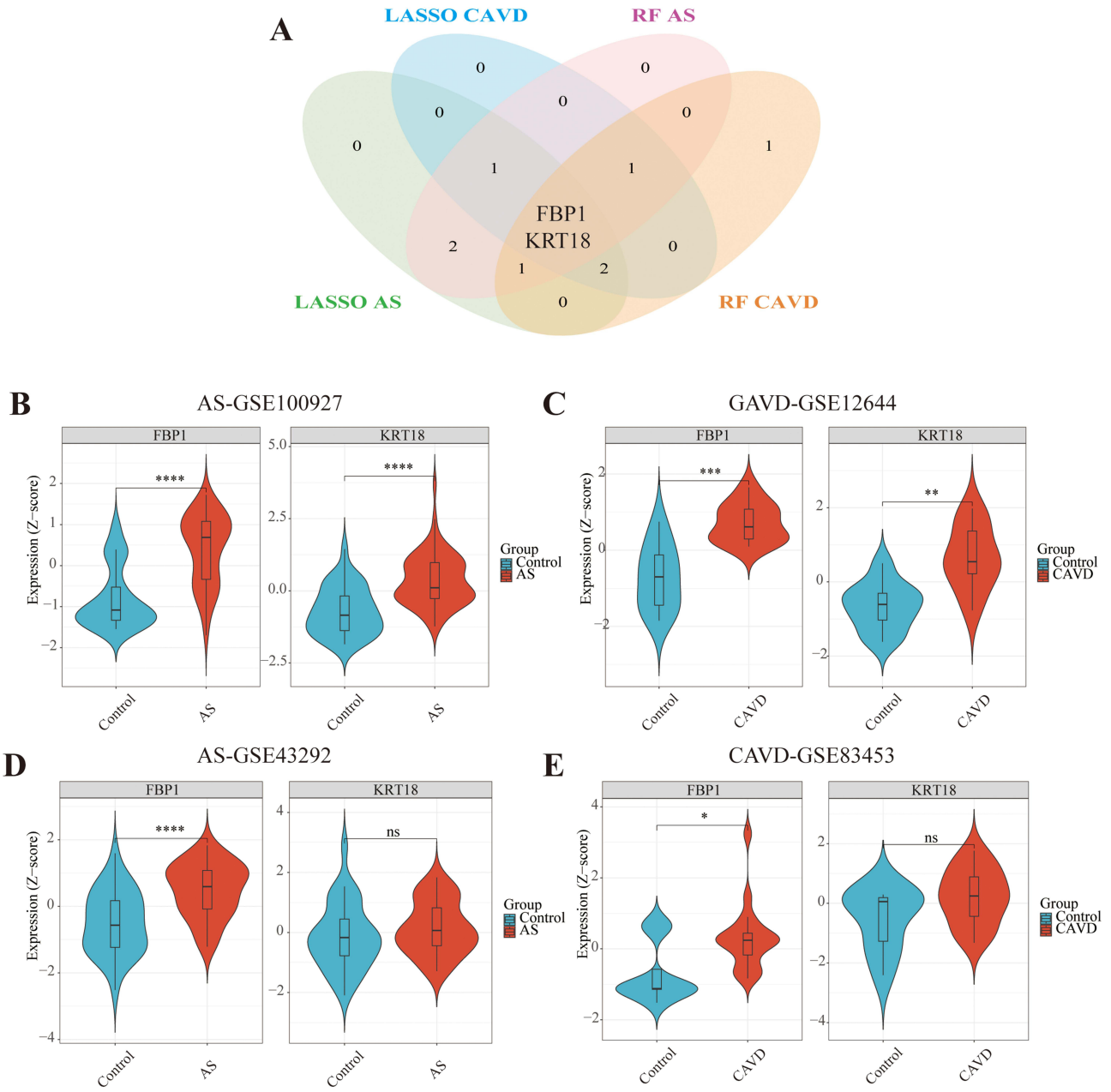

Figure 5 Identification and expression validation of candidate genes. (**A**) Intersection of LASSO and RF results across AS and CAVD cohorts identifying FBP1 and KRT18 as common candidate genes. (**B–E**) Expression profiles of candidate genes. Significance: P < 0.05 (*), P < 0.01 (**), P < 0.001 (***), P < 0.0001 (****); ns = not significant.

Regulatory Network Exploration of FBP1

To elucidate the contribution of the hub gene to the comorbidity of AS and CAVD, GSEA analysis was performed for FBP1. In the AS, immune and inflammatory signatures predominated, accompanied by marked activation of lysosomal pathways (Figure 8A and B). Given that lysosomal cathepsins degrade oxidised LDL and promote foam-cell formation, the data imply reciprocal reinforcement between disordered lipid metabolism and inflammation during atherogenesis. In the CAVD datasets, metabolic reprogramming was more prominent, with significant enrichment in ubiquitin-mediated proteolysis and calcium-signalling cascades, indicating that perturbations in protein homeostasis and calcium handling may accelerate valvular calcification. Pronounced activation of Toll-like-receptor signalling further suggests tight coupling between metabolic disturbance and innate immunity in CAVD (Figure 8C and D). Given the central role of VSMCs in atherogenesis, we assessed FBP1–VSMC phenotype coupling by correlating FBP1 expression with markers of contractility, inflammation, osteogenic calcification, proliferation, and senescence in two AS cohorts (GSE100927, GSE43292). After quantile normalization,

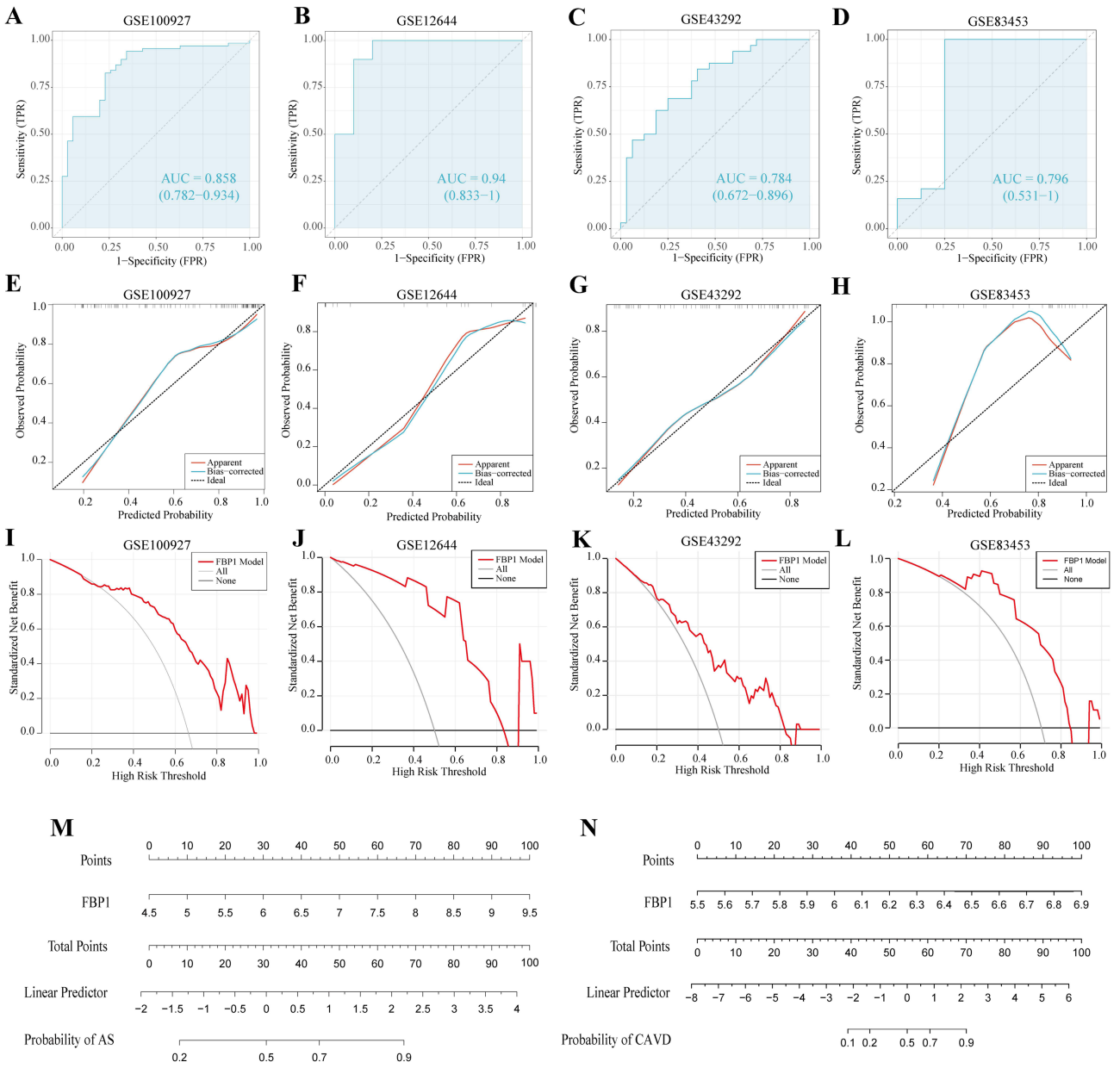

Figure 6 Diagnostic performance of the FBP1-based prediction model. (**A–D**) ROC curves demonstrating the predictive accuracy of FBP1 in AS and CAVD datasets. (**E–H**) Calibration curves showing agreement between predicted and actual outcomes in both diseases. (**I–L**) Decision curve analyses indicating clinical net benefit of the FBP1-based model in AS and CAVD. (**M–N**) Nomogram and schematic representations of AS and CAVD prediction models incorporating FBP1 expression.

Spearman correlations showed that FBP1 was negatively associated with contractile markers (TAGLN, MYH11, CNN1) and positively associated with osteogenic, inflammatory, and proliferative markers (eg, RUNX2, ICAM1, MKI67), as well as senescence markers (CDKN2A), with multiple associations reaching nominal significance (Figure 8E and F).

Collectively, the results reveal a shared immune–metabolic interface in the two disorders while underscoring disease-specific pathogenic axes. The regulatory landscape of FBP1 was then delineated. The gene is situated on chromosome 9 (Figure 9A). A protein–protein-interaction network constructed in STRING positioned FBP1 at the core of glycolytic and broader glucose-metabolic circuitry (Figure 9B). Intersection of transcription-factor predictions from ENCODE, hTFtarget and KnockTF identified four regulators consistently linked to FBP1 (Figure 9C). The potential microRNAs of FBP1 were predicted using the mirwalk database (Supplementary Table 3). In addition, we provide a structured, column-based summary of FBP1-targeting miRNAs, including the miRNA name, database, binding score or ΔG, genomic region, and start and end coordinates, in Supplementary Excel 2. Integration of these transcription factors

https://doi.org/10.2147/JIR.S540540

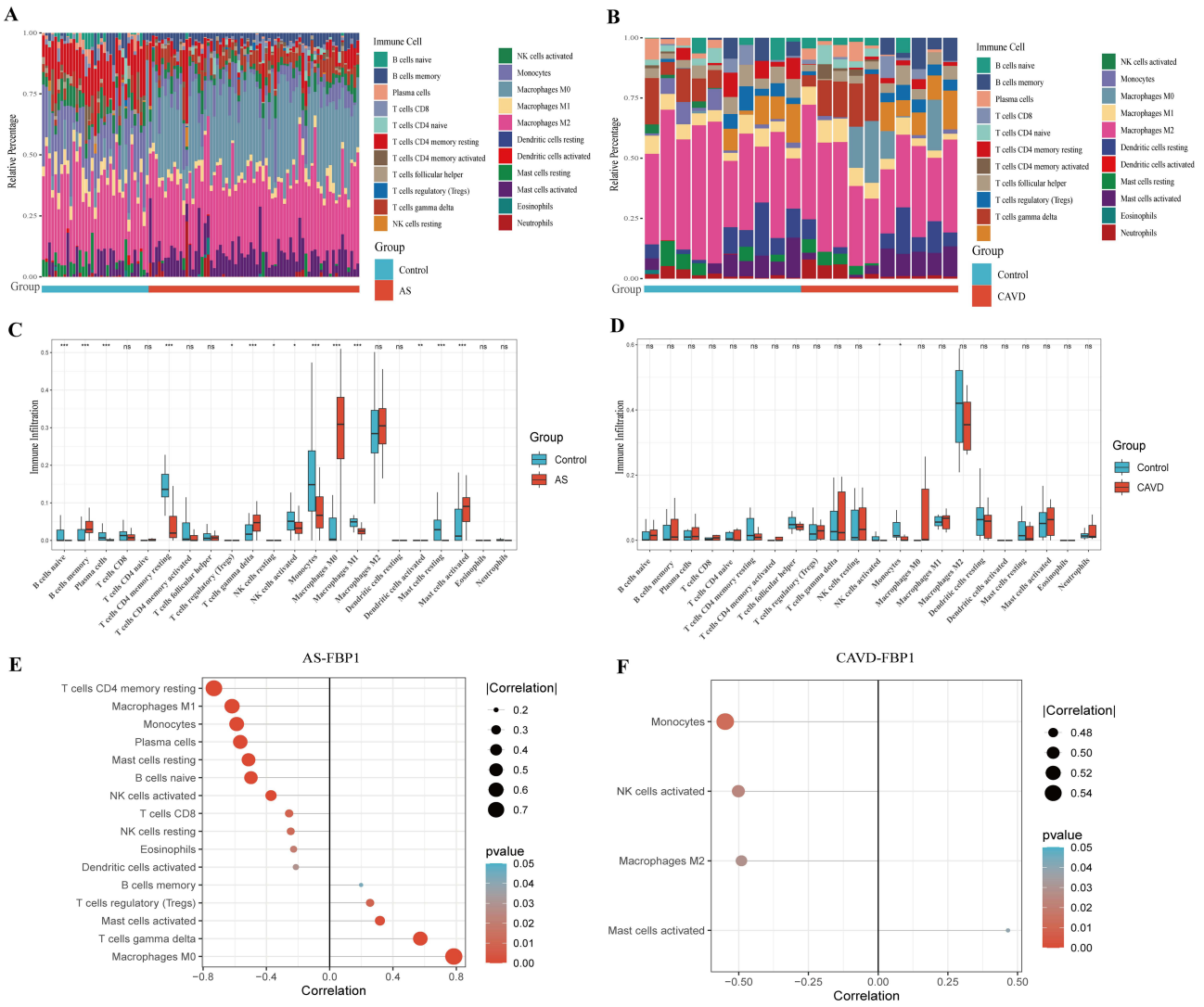

Figure 7 Immune infiltration analysis and correlation with FBP1 expression. (**A**) Relative proportions of 22 immune-cell subsets in AS and controls. (**B**) Relative proportions of 22 immune-cell subsets in CAVD and controls. (**C**) Differential immune-cell abundances in AS vs controls. (**D**) Differential immune-cell abundances in CAVD vs controls. (**E**) Spearman correlations between FBP1 expression and immune-cell fractions in AS. (**F**) Spearman correlations between FBP1 expression and immune-cell fractions in CAVD. Significance: P < 0.05 (*), P < 0.01 (**), P < 0.001 (***); ns = not significant.

with predicted microRNAs yielded a multilayer regulatory network in which FBP1 occupies a central node, illustrating coordinated transcriptional and post-transcriptional control (Figure 9D).

Therapeutic Targeting Potential of FBP1

Candidate FBP1-targeting compounds were first prioritised in Enrichr, and the four most significantly enriched molecules-chrysin, myricetin, kaempferol and apigenin were advanced to molecular-docking analysis. Ligand structures were retrieved from PubChem, and the FBP1 crystal structure was obtained from the Protein Data Bank. Docking performed with AutoDock Vina yielded binding affinities below −8 kcal/mol for all four ligands, indicating strong interaction potential (Supplementary Table 4). To benchmark docking performance, we additionally included control compounds docked under identical receptor/grid settings: a positive control (FBPase-IN-1; Vina score −9.0 kcal/mol) and a negative control (glucose; −5.4 kcal/mol); these results, together with compound source and docking parameters, are reported in Supplementary Table 4.

The docking results are illustrated in Figure 10, which includes both 3D binding conformations and corresponding 2D interaction diagrams. Each compound was found to bind within the active site pocket of FBP1, forming multiple

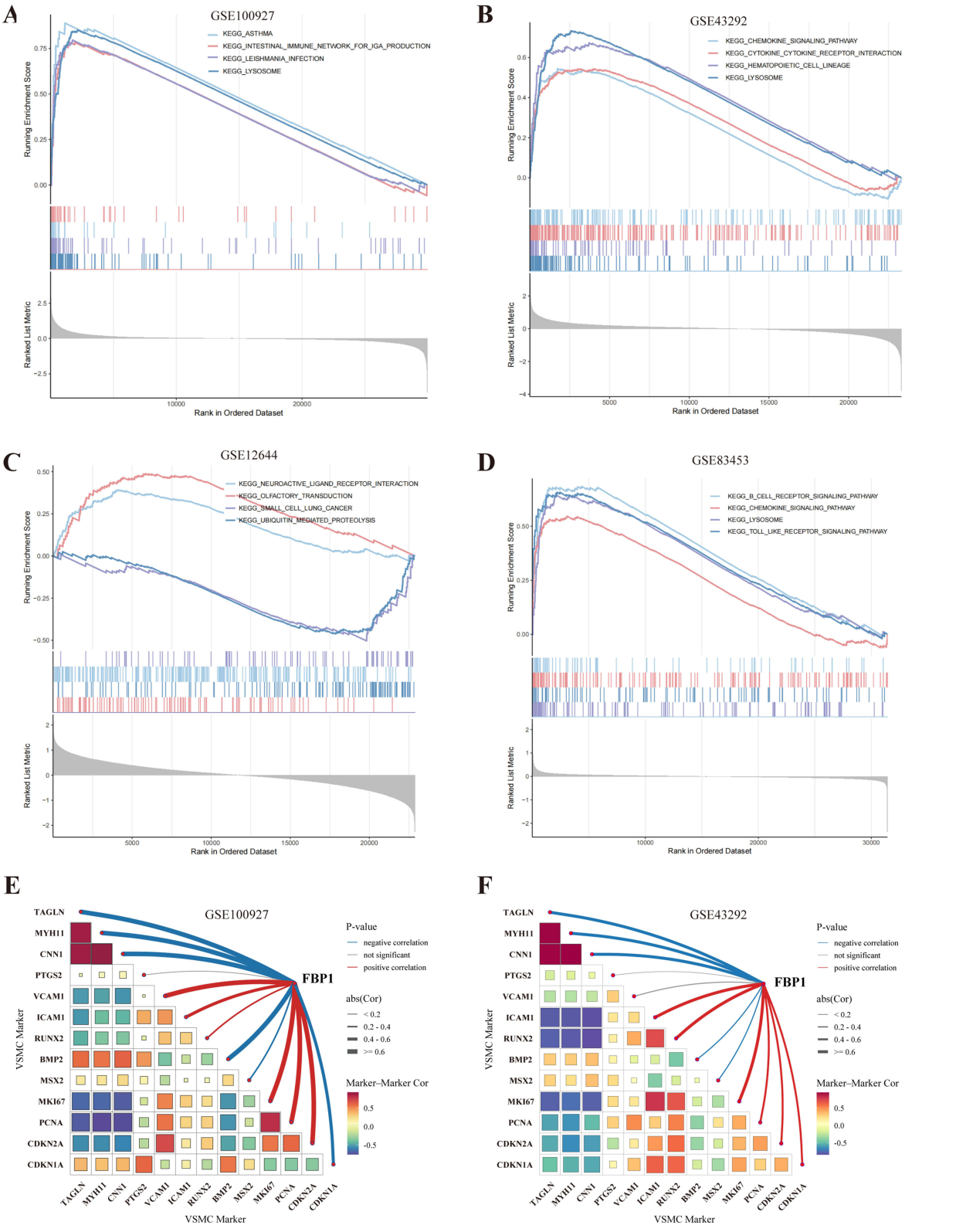

Figure 8 Pathway enrichment and VSMC phenotype coupling of FBP1. (**A** and **B**) GSEA of FBP1 in AS datasets. (**C** and **D**) GSEA of FBP1 in CAVD datasets. (**E** and **F**) FBP1–VSMC marker correlations in AS datasets (Spearman, P<0.05).

https://doi.org/10.2147/JIR.S540540

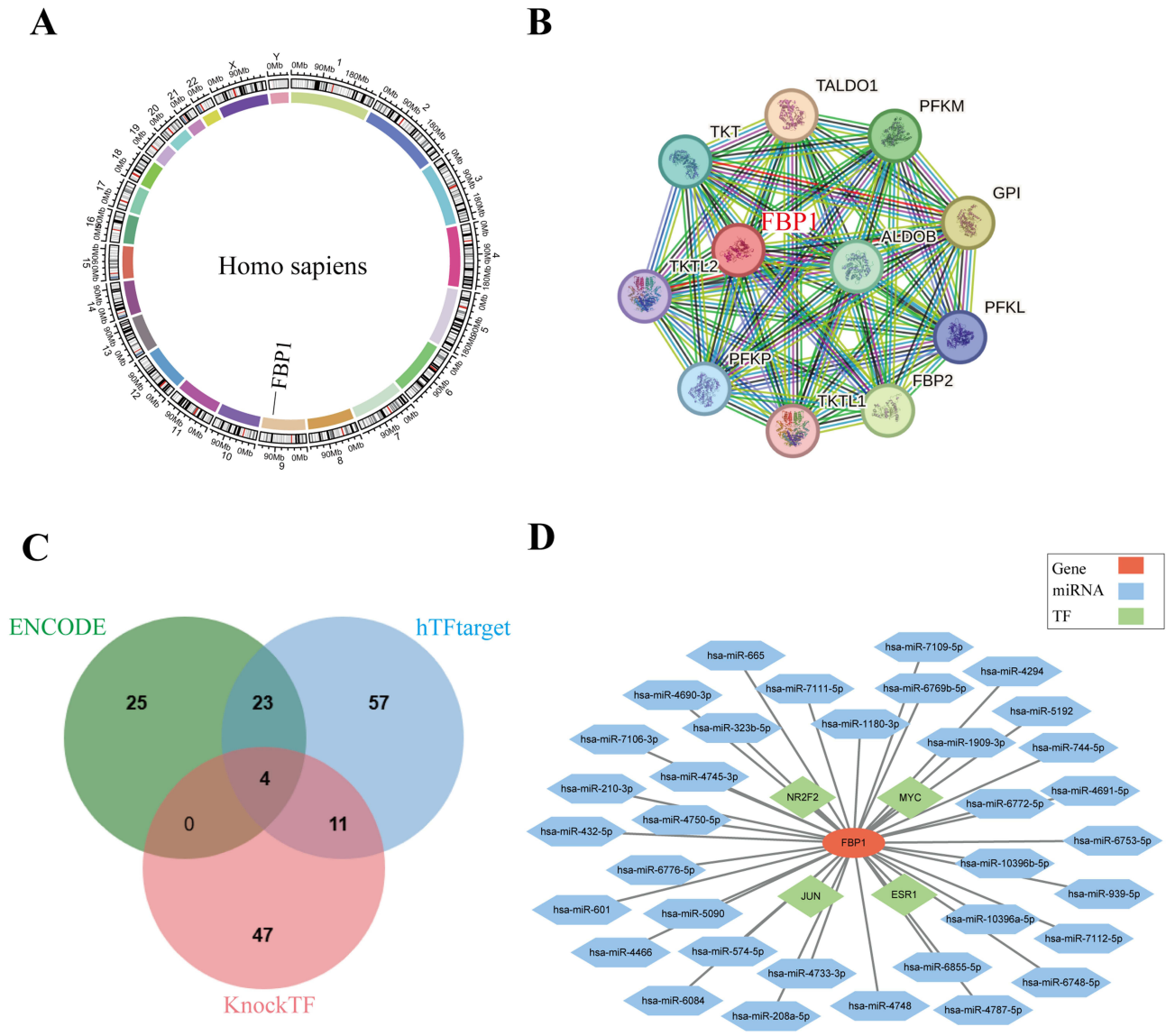

Figure 9 Regulatory landscape of FBP1. (**A**) Chromosomal location of FBP1. (**B**) Protein-protein interaction network showing FBP1-centered metabolic associations. (**C**) Venn diagram of transcription factors predicted by ENCODE, hTFtarget, and KnockTF. (**D**) Integrated regulatory network of FBP1 involving transcription factors and microRNAs.

stabilizing interactions. Chrysin (Figure 10A and B) exhibited hydrogen bonding and hydrophobic contacts with several key residues. Myricetin (Figure 10C and D) formed a denser hydrogen bond network, suggesting strong binding affinity. Kaempferol (Figure 10E and F) displayed the most extensive interaction profile, including multiple hydrogen bonds and π–π stacking interactions. Similarly, apigenin (Figure 10G and H) demonstrated favorable binding, with a combination of van der Waals forces, hydrogen bonds, and electrostatic interactions.

Experimental Validation of FBP1

Building on the bioinformatic findings, we examined clinical specimens by histopathology and expression assays. Representative sections were stained with hematoxylin–eosin (HE) and Oil Red O (ORO). Paired common carotid artery (CCA) samples from the same individuals demonstrated a clear transition from CCA—less-affected intima (CCA-LA) to CCA—advanced atherosclerotic intima (CCA-Adv), the latter exhibiting pronounced intimal thickening, complex plaque architecture, and abundant neutral-lipid deposition (Figure 11A). In the lower-extremity cohort, femoral arteries with

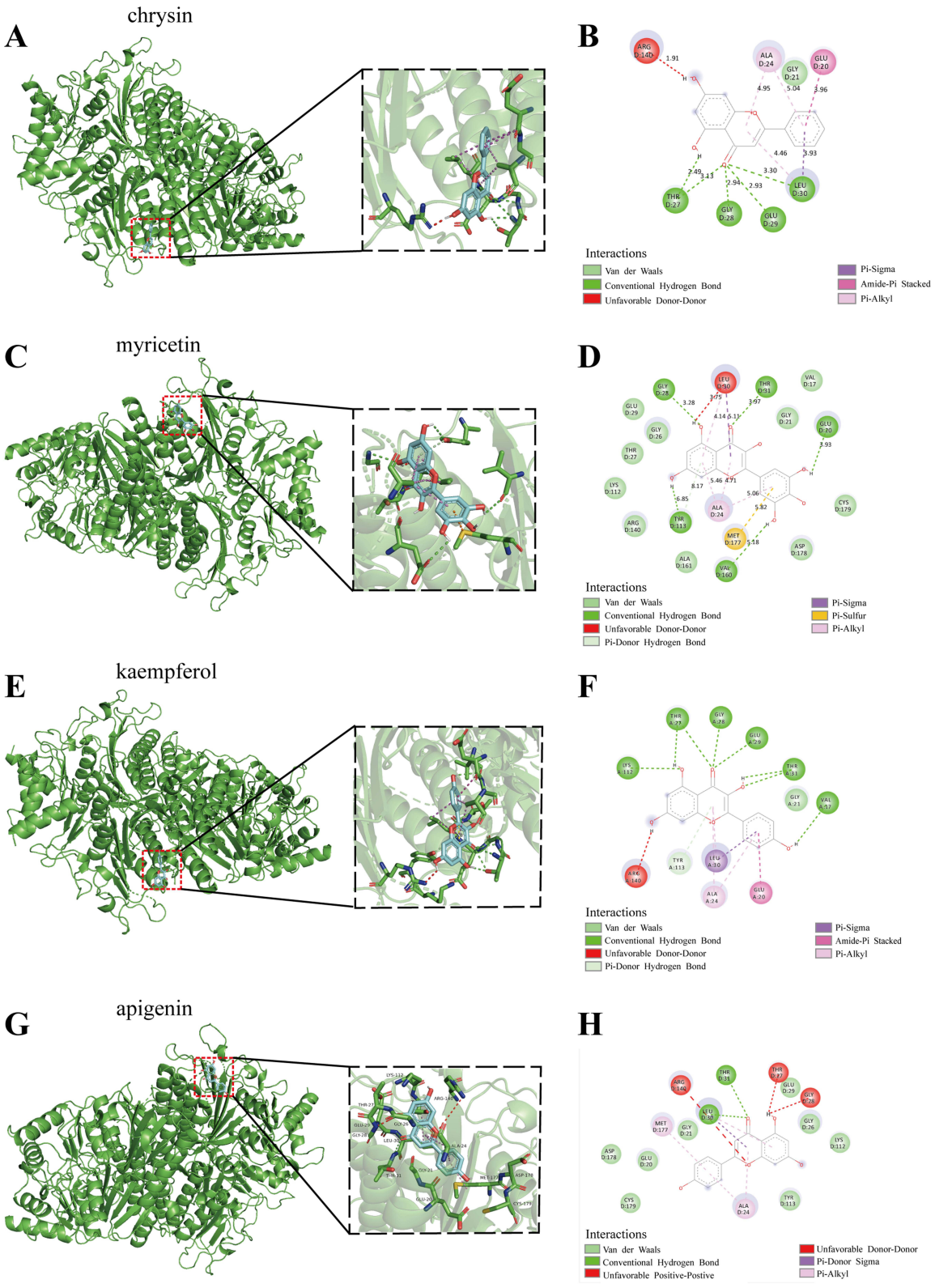

Figure 10 Molecular docking analysis of candidate compounds targeting FBP1. (**A–H**) Docking results for chrysin, myricetin, kaempferol, and apigenin with FBP1.

https://doi.org/10.2147/JIR.S540540

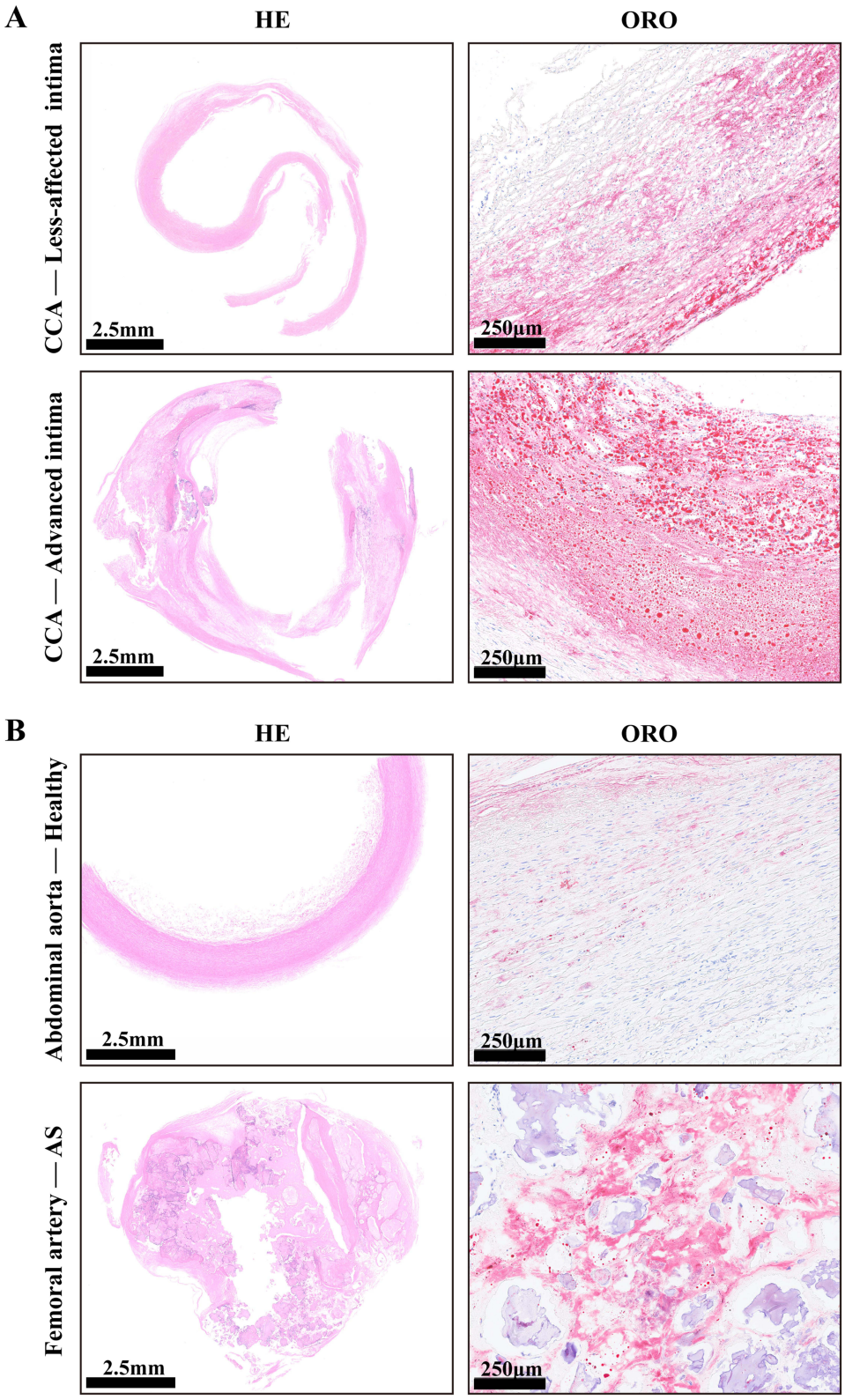

Figure 11 HE and Oil Red O staining of atherosclerotic arteries from different sites. (**A**) Common carotid artery—less-affected intima (CCA-LA): HE, Scale bar: 2.5 mm; Oil Red O (ORO), Scale bar: 250 μm. Common carotid artery—advanced atherosclerotic intima (CCA-Adv): HE, Scale bar: 2.5 mm; ORO, Scale bar: 250 μm. (**B**) Abdominal aorta—healthy: HE, Scale bar: 2.5 mm; ORO, Scale bar: 250 μm. Femoral artery—atherosclerosis: HE, Scale bar: 2.5 mm; ORO, Scale bar: 250 μm.

atherosclerosis showed marked ORO-positive lipid accumulation with extensive calcific foci, whereas post-mortem healthy abdominal aorta displayed only minimal lipid and preserved wall architecture (Figure 11B).

Consistent with the bioinformatics results, Western blot showed higher FBP1 protein in lower-extremity arteriosclerosis obliterans (LE-ASO) arteries and in CCA—advanced atherosclerotic intima (CCA-Adv) relative to their corresponding controls, with densitometric analysis confirming statistical significance (Figure 12A–D). Likewise, CAVD valves exhibited increased FBP1 protein compared with controls (Figure 12E and F). RT-qPCR further demonstrated elevated FBP1 mRNA in LE-ASO and CCA-Adv versus controls (Figure 12G and H) and in CAVD versus NC (Figure 12I). Collectively, these data indicate that FBP1 is upregulated in both atherosclerotic vascular lesions and calcific aortic valves, supporting its candidacy as a shared immunometabolic biomarker bridging AS and CAVD.

Discussion

In ageing populations, the incidence and mortality of AS and CAVD continue to rise as risk factors accumulate.[3,37] Despite advances in our understanding, current diagnostic and therapeutic approaches remain inadequate. AS frequently remains undetected until acute cardiovascular events occur,[38] and CAVD diagnosis often relies on echocardiography, detecting only advanced stenosis.[39] Pharmacological interventions capable of halting disease progression are limited. Surgical treatments, including vascular reconstruction in AS and valve replacement in CAVD,[40,41] are invasive and expensive, underscoring the urgent need for effective biomarkers and therapies targeting the common molecular pathways of both diseases. Although the two conditions are generally treated as separate clinical entities, mounting evidence indicates substantial overlap in their pathogenic mechanisms.[42] Both share major risk factors (hypertension, hypercholesterolaemia, smoking, age) and the hallmarks of chronic inflammation and metabolic dysregulation.[1,8,10] Recent work highlights a bidirectional crosstalk between metabolic reprogramming and immune-mediated inflammation: metabolic disturbances impair immune-cell function, accelerating structural injury and remodelling of arterial walls and valvular leaflets, whereas sustained inflammation not only fosters plaque development in AS but also exacerbates calcification and stenosis in CAVD.[6,43,44] Because most cases are diagnosed at advanced stages—when plaque instability or severe valvular obstruction has occurred—defining shared molecular pathways is essential for earlier detection and more effective intervention.

We identified 147 CGs common to AS and CAVD. Functional enrichment revealed widespread dysregulation, relative to normal tissue, in immune-inflammatory and metabolism-related pathways. Prior work suggests that inflammation is a driver, not merely a downstream consequence, of disease progression. Disordered inflammatory signalling induces metabolic reprogramming, whereas aberrant metabolites further amplify inflammation, establishing a vicious cycle.[45] By integrating two machine-learning algorithms,[28] we ultimately prioritised a single biomarker—FBP1. FBP1 was consistently upregulated in discovery and validation datasets, with ROC AUCs >0.70 across cohorts, indicating good discrimination. Calibration curves demonstrated close agreement between predicted and observed outcomes, and decision-curve analysis indicated clear net clinical benefit across a broad risk threshold. A nomogram that integrates FBP1 transcript level with clinical covariates provides a practical tool for individualised risk stratification.

FBP1 is the rate-limiting enzyme of gluconeogenesis and a critical regulator of energy homeostasis.[46] In atherosclerotic plaques, heavily infiltrated macrophages exhibit a "high-glycolysis/low-oxidative-phosphorylation" phenotype that corresponds closely to elevated expression of this glycolytic enzyme.[47] Early studies have shown that FBP1 can activate immune-related pathways in AS, including interferon-γ and PD-1 signalling cascades, and can influence the behaviour of M0 macrophages, γδ T cells, plasma cells, and monocytes.[48] Although data for CAVD remain scarce, the disorder similarly features mutually reinforcing metabolic stress and inflammation. Early-stage CAVD is characterised by leaflet thickening, fibrosis, and immune-cell infiltration, ultimately progressing to calcium deposition. Hypoxia within thickened cusps up-regulates HIF-1α and HIF-2α, and hypoxia-induced glycolysis with local lactate accumulation is likely to ensue.[49] Consistent with these observations, our immune-cell deconvolution showed that high FBP1 expression is strongly associated with pro-inflammatory subsets—particularly M0 macrophages and activated mast cells—indicating that FBP1 may sustain the inflammation–metabolism feed-forward loop. Endothelial dysfunction is regarded as the initiating event in degenerative vascular disease,[50] and endothelial FBP1 expression has recently attracted interest. Retinoic acid, for example, can up-regulate FBP1 transcription via the nuclear receptor RAR, redirecting endothelial

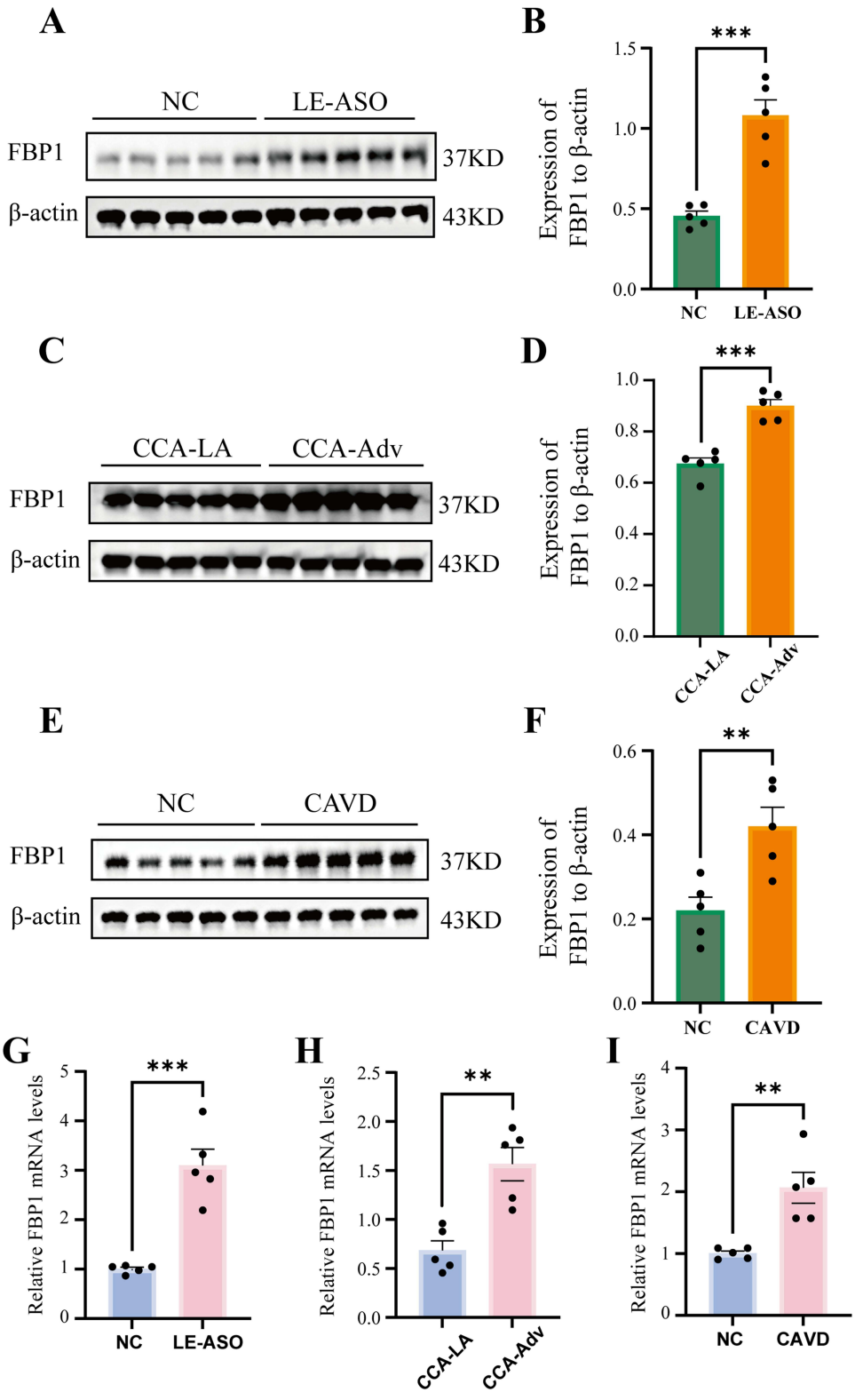

Figure 12 Experimental validation of FBP1 expression in AS and CAVD tissues. (**A** and **B**) Western blot of FBP1 in lower-extremity arteriosclerosis obliterans (LE-ASO) vs normal controls (NC); densitometry. (**C** and **D**) FBP1 in common carotid artery—advanced atherosclerotic intima (CCA-Adv) vs less-affected intima (CCA-LA); densitometry. (**E** and **F**) FBP1 in CAVD vs NC; densitometry. (**G**) RT-qPCR of FBP1 mRNA in LE-ASO vs NC. (**H**) RT-qPCR in CCA-Adv vs CCA-LA. (**I**) RT-qPCR in CAVD vs NC. Data: mean ± SEM (n = 5 per group). Significance: $P < 0.01$ (**), $P < 0.001$ (***).

metabolism toward gluconeogenesis and mitochondrial oxidation while suppressing proliferation and migration.[51] In other experimental systems, FBP1 over-expression attenuates NRF2-mediated antioxidant defences and exacerbates oxidative stress.[52] If analogous mechanisms prevail in vascular endothelium, dysregulated FBP1 could weaken antioxidant protection and provoke chronic inflammation, thereby aggravating endothelial injury.

GSEA demonstrated that FBP1 is deeply involved in both immune and metabolic pathways. Although the specific pathways enriched in AS and CAVD differ, the two diseases share overarching immune–metabolic dysregulation, with the lysosome pathway emerging as particularly prominent across multiple datasets. Lysosomes are crucial for antigen processing and lipid metabolism: in AS, lysosomal cathepsins facilitate foam-cell formation by degrading oxidised LDL;[53] in CAVD, lysosomal dysfunction may amplify innate immune activation and calcification.[54] Thus, lysosomes constitute a molecular hub linking immune and metabolic responses in AS–CAVD comorbidity.

We next constructed an FBP1-centred gene-regulatory network. Cross-referencing multiple databases identified several transcription factors and microRNAs that converge on FBP1, revealing coordinated control at transcriptional and post-transcriptional levels. These regulators provide multiple leverage points for therapeutic modulation. Using DSigDB for drug-signature enrichment combined with AutoDock Vina docking, we prioritised four flavonoids—chrysin, myricetin, kaempferol, and apigenin—with binding energies below –8 kcal mol^{-1}, indicative of strong interaction potential. All four compounds possess established antioxidant and anti-inflammatory properties,[55–58] and their predicted ability to target FBP1 suggests a dual capacity to correct metabolic imbalance and attenuate inflammation. These candidates warrant further validation in cellular and animal models.

Several limitations must be acknowledged. First, our experimental validation used small clinical cohorts (n = 5 per group), which limits statistical power, widens confidence intervals, and increases the risk of type I/II error; thus, the findings should be considered preliminary. Future work will include larger, prospectively powered, multi-centre cohorts with predefined endpoints, independent replication, and expanded functional studies to strengthen inference. Second, our inferences about FBP1 regulation by miRNAs and transcription factors are based on in-silico predictions and currently lack experimental confirmation. We will pursue targeted validation of miRNA–FBP1 binding and TF occupancy, conduct functional perturbation studies to test regulatory effects. Finally, functional validation of the candidate flavonoids will require extensive basic science and preclinical studies.

Conclusion

Despite these constraints, the present work offers new insight into the pathological nexus between immune dysregulation and metabolic dysfunction in vascular disease. Clinically, FBP1 emerges as a promising dual biomarker and therapeutic target for AS and CAVD, paving the way for precision strategies that simultaneously address inflammatory and metabolic drivers of these degenerative disorders.

Data Sharing Statement

The datasets presented in this study can be found in online repositories. The names of the repository/repositories and accession number(s) can be found in the article/ Supplementary Material.

Ethics Statement

The studies involving humans were approved by The Ethics Committee of the Affiliated Hospital of Qingdao University (No.QYFY WZLL 29793). The studies were conducted in accordance with the local legislation and institutional requirements. The participants provided their written informed consent to participate in this study.

Consent for Publication

The authors consent to the publication of this research and confirm that all data, figures, and materials in the manuscript are accurate and have not been previously published elsewhere. All authors have approved the final version of the manuscript for publication.

Acknowledgments

Haowen Xu and Yifan Xu are co-first authors for this study. Rstudio was used to create Graphics. All claims expressed in this article are solely those of the authors and do not necessarily represent those of their affiliated organizations, or those of the publisher, the editors and the reviewers. Any product that may be evaluated in this article, or claim that may be made by its manufacturer, is not guaranteed or endorsed by the publisher.

Author Contributions

All authors made a significant contribution to the work reported, whether that is in the conception, study design, execution, acquisition of data, analysis and interpretation, or in all these areas; took part in drafting, revising or critically reviewing the article; gave final approval of the version to be published; have agreed on the journal to which the article has been submitted; and agree to be accountable for all aspects of the work.

Funding

The authors declare that no financial support was received for the research, authorship, and/or publication of this article.

Disclosure

The authors declare that the research was conducted in the absence of any commercial or financial relationships that could be construed as a potential conflict of interest.

References

1. Wali JA, Jarzebska N, Raubenheimer D, Simpson SJ, Rodionov RN, O'Sullivan JF. Cardio-metabolic effects of high-fat diets and their underlying mechanisms—a narrative review. *Nutrients*. 2020;12(5):1505. doi:10.3390/nu12051505
2. Wang S, Ren J. Obesity paradox in aging: from prevalence to pathophysiology. *Prog Cardiovasc Diseases*. 2018;61:182–189. doi:10.1016/j.pcad.2018.07.011
3. Nedkoff L, Briffa T, Zemedikun D, Herrington S, Wright FL. Global trends in atherosclerotic cardiovascular disease. *Clin Ther*. 2023;45:1087–1091. doi:10.1016/j.clinthera.2023.09.020
4. Small A, Kiss D, Giri J, et al. Biomarkers of calcific aortic valve disease. *Arterioscler Thromb Vasc Biol*. 2017;37:623–632. doi:10.1161/ATVBAHA.116.308615
5. Otto CM, Newby DE, Hillis GS. Calcific aortic stenosis: a review. *JAMA*. 2024;332:2014–2026. doi:10.1001/jama.2024.16477
6. Porsch F, Binder CJ. Autoimmune diseases and atherosclerotic cardiovascular disease. *Nat Rev Cardiol*. 2024;21:780–807. doi:10.1038/s41569-024-01045-7
7. Wang JC, Bennett M. Aging and atherosclerosis. *Circu Res*. 2012;111:245–259. doi:10.1161/CIRCRESAHA.111.261388
8. Scott AJ, Simon LR, Hutson HN, Porras AM, Masters KS. Engineering the aortic valve extracellular matrix through stages of development, aging, and disease. *J Mol Cell Cardiol*. 2021;161:1–8. doi:10.1016/j.yjmcc.2021.07.009
9. Blaser MC, Bäck M, Lüscher TF, Aikawa E. Calcific aortic stenosis: omics-based target discovery and therapy development. *Eur Heart J*. 2025;46:620–634. doi:10.1093/eurheartj/ehae829
10. Castillo-Núñez Y, Almeda-Valdes P, González-Gálvez G, Arechavaleta-Granell MDR. Metabolic dysfunction-associated steatotic liver disease and atherosclerosis. *Curr Diab Rep*. 2024;24:158–166. doi:10.1007/s11892-024-01542-6
11. Ajoolabady A, Pratico D, Lin L, et al. Inflammation in atherosclerosis: pathophysiology and mechanisms. *Cell Death Dis*. 2024;15:817. doi:10.1038/s41419-024-07166-8
12. Perez KA, Deppe DW, Filas A, Singh SA, Aikawa E. Multimodal analytical tools to enhance mechanistic understanding of aortic valve calcification. *Am J Pathol*. 2024;194:539–550. doi:10.1016/j.ajpath.2023.06.017
13. Sud K, Narula N, Aikawa E, et al. The contribution of amyloid deposition in the aortic valve to calcification and aortic stenosis. *Nat Rev Cardiol*. 2023;20:418–428. doi:10.1038/s41569-022-00818-2
14. Di Nubila A, Dilella G, Simone R, Barbieri SS. Vascular extracellular matrix in atherosclerosis. *Int J Mol Sci*. 2024;25:12017. doi:10.3390/ijms252212017
15. Ference BA, Braunwald E, Catapano AL. The LDL cumulative exposure hypothesis: evidence and practical applications. *Nat Rev Cardiol*. 2024;21:701–716. doi:10.1038/s41569-024-01039-5
16. Nsaibia MJ, Devendran A, Goubaa E, Bouitbir J, Capoulade R, Bouchareb R. Implication of lipids in calcified aortic valve pathogenesis: why did statins fail? *J Clin Med*. 2022;11:3331. doi:10.3390/jcm11123331
17. Moncla L-HM, Briend M, Bossé Y, Mathieu P. Calcific aortic valve disease: mechanisms, prevention and treatment. *Nat Rev Cardiol*. 2023;20:546–559. doi:10.1038/s41569-023-00845-7
18. Poznyak A, Grechko AV, Poggio P, Myasoedova VA, Alfieri V, Orekhov AN. The diabetes mellitus-atherosclerosis connection: the role of lipid and glucose metabolism and chronic inflammation. *Int J Mol Sci*. 2020;21:1835. doi:10.3390/ijms21051835
19. Libby P, Buring JE, Badimon L, et al. Atherosclerosis. *Nat Rev Dis Primers*. 2019;5:56. doi:10.1038/s41572-019-0106-z
20. Kostyunin A, Mukhamadiyarov R, Glushkova T, et al. Ultrastructural pathology of atherosclerosis, calcific aortic valve disease, and bioprosthetic heart valve degeneration: commonalities and differences. *Int J Mol Sci*. 2020;21:7434. doi:10.3390/ijms21207434

21. Barrett T, Wilhite SE, Ledoux P, et al. NCBI GEO: archive for functional genomics data sets--update. *Nucleic Acids Res*. 2012;41:D991–D995. doi:10.1093/nar/gks1193
22. Bai F, Wang C, Fan X, et al. Novel biomarkers related to oxidative stress and immunity in chronic kidney disease. *Heliyon*. 2024;10:e27754. doi:10.1016/j.heliyon.2024.e27754
23. Ritchie ME, Phipson B, Wu D, et al. limma powers differential expression analyses for RNA-sequencing and microarray studies. *Nucleic Acids Res*. 2015;43:e47–e47. doi:10.1093/nar/gkv007
24. The Gene Ontology Consortium. Gene ontology consortium: going forward. *Nucleic Acids Res*. 2015;43:D1049–D1056. doi:10.1093/nar/gku1179
25. Ogata H, Goto S, Sato K, Fujibuchi W, Bono H, Kanehisa MKEGG. Kyoto encyclopedia of genes and genomes. *Nucleic Acids Res*. 1999;27:29–34. doi:10.1093/nar/27.1.29
26. Wu T, Hu E, Xu S, et al. clusterProfiler 4.0: a universal enrichment tool for interpreting omics data. *Innovation*. 2021;2:100141. doi:10.1016/j.xinn.2021.100141
27. Subramanian A, Tamayo P, Mootha VK, et al. Gene set enrichment analysis: a knowledge-based approach for interpreting genome-wide expression profiles. *Proc Natl Acad Sci U S A*. 2005;102:15545–15550. doi:10.1073/pnas.0506580102
28. Xu Y, Guo P, Wang G, et al. Integrated analysis of single-cell sequencing and machine learning identifies a signature based on monocyte/macrophage hub genes to analyze the intracranial aneurysm associated immune microenvironment. *Front Immunol*. 2024;15:1397475. doi:10.3389/fimmu.2024.1397475
29. Hu J, Szymczak S. A review on longitudinal data analysis with random forest. *Brief Bioinform*. 2023;24:bbad002. doi:10.1093/bib/bbad002
30. pROC: an open-source package for R and S+ to analyze and compare ROC curves - PubMed. Available from: https://pubmed.ncbi.nlm.nih.gov/21414208/. Accessed April 23, 2025.
31. Shannon P, Markiel A, Ozier O, et al. Cytoscape: a software environment for integrated models of biomolecular interaction networks. *Genome Res*. 2003;13:2498–2504. doi:10.1101/gr.1239303
32. Sticht C, De La Torre C, Parveen A, Gretz N. miRWalk: an online resource for prediction of microRNA binding sites. *PLoS One*. 2018;13:e0206239. doi:10.1371/journal.pone.0206239
33. Feng C, Song C, Song S, et al. KnockTF 2.0: a comprehensive gene expression profile database with knockdown/knockout of transcription (co-) factors in multiple species. *Nucleic Acids Res*. 2024;52. doi:10.1093/nar/gkad1016
34. Yoo M, Shin J, Kim J, et al. DSigDB: drug signatures database for gene set analysis. *Bioinformatics*. 2015;31:3069–3071. doi:10.1093/bioinformatics/btv313
35. Liu Y, Yang X, Gan J, Chen S, Xiao Z-X, Cao Y. CB-Dock2: improved protein-ligand blind docking by integrating cavity detection, docking and homologous template fitting. *Nucleic Acids Res*. 2022;50:W159–W164. doi:10.1093/nar/gkac394
36. Yu B, Wang Q, Zhang L, et al. Ebselen improves fungal keratitis through exerting anti-inflammation, anti-oxidative stress, and antifungal effects. *Redox Biol*. 2024;73:103206. doi:10.1016/j.redox.2024.103206
37. Yi B, Zeng W, Lv L, Hua P. Changing epidemiology of calcific aortic valve disease: 30-year trends of incidence, prevalence, and deaths across 204 countries and territories. *Aging*. 2021;13:12710–12732. doi:10.18632/aging.202942
38. Libby P, Bornfeldt KE, Tall AR. Atherosclerosis: successes, surprises, and future challenges. *Circ Res*. 2016;118:531–534. doi:10.1161/CIRCRESAHA.116.308334
39. Yadgir S, Johnson CO, Aboyans V, et al. Global, regional, and national burden of calcific aortic valve and degenerative mitral valve diseases, 1990–2017. *Circulation*. 2020;141(21):1670–1680. doi:10.1161/CIRCULATIONAHA.119.043391
40. Farber A, Menard MT, Conte MS, et al. Surgery or endovascular therapy for chronic limb-threatening ischemia. *N Engl J Med*. 2022;387:2305–2316. doi:10.1056/NEJMoa2207899
41. Jain H, Goyal A, Khan ATMA, et al. Insights into calcific aortic valve stenosis: a comprehensive overview of the disease and advancing treatment strategies. *Ann Med Surg*. 2024;86:3577–3590. doi:10.1097/MS9.0000000000002106
42. Hafiane A, Pisaturo A, Favari E, Bortnick AE. Atherosclerosis, calcific aortic valve disease and mitral annular calcification: same or different? *Int J Cardiol*. 2025;420:132741. doi:10.1016/j.ijcard.2024.132741
43. Galkina E, Ley K. Immune and inflammatory mechanisms of atherosclerosis (*). *Annu Rev Immunol*. 2009;27:165–197. doi:10.1146/annurev.immunol.021908.132620
44. Rajamannan NM, Evans FJ, Aikawa E, et al. Calcific aortic valve disease: not simply a degenerative process a review and agenda for research from the national heart and lung and blood institute aortic stenosis working group. *Circulation*. 2011;124:1783–1791. doi:10.1161/CIRCULATIONAHA.110.006767
45. Arifuzzaman M, Collins N, Guo C-J, Artis D. Nutritional regulation of microbiota-derived metabolites: implications for immunity and inflammation. *Immunity*. 2024;57:14–27. doi:10.1016/j.immuni.2023.12.009
46. Gu L, Zhu Y, Watari K, et al. Fructose-1,6-bisphosphatase is a nonenzymatic safety valve that curtails AKT activation to prevent insulin hyperresponsiveness. *Cell Metab*. 2023;35:1009–1021.e9. doi:10.1016/j.cmet.2023.03.021
47. Viola A, Munari F, Sánchez-Rodríguez R, Scolaro T, Castegna A. The metabolic signature of macrophage responses. *Front Immunol*. 2019;10. doi:10.3389/fimmu.2019.01462
48. Shen Y, Xu L, Tang X, et al. Identification of potential therapeutic targets for atherosclerosis by analysing the gene signature related to different immune cells and immune regulators in atheromatous plaques. *BMC Med Genomics*. 2021;14:145. doi:10.1186/s12920-021-00991-2
49. Bouhamida E, Morciano G, Pedriali G, et al. The complex relationship between hypoxia signaling, mitochondrial dysfunction and inflammation in calcific aortic valve disease: insights from the molecular mechanisms to therapeutic approaches. *Int J Mol Sci*. 2023;24:11105. doi:10.3390/ijms241311105
50. Xu S, Ilyas I, Little PJ, et al. Endothelial dysfunction in atherosclerotic cardiovascular diseases and beyond: from mechanism to pharmacotherapies. *Pharmacol Rev*. 2021;73:924–967. doi:10.1124/pharmrev.120.000096
51. Yang Z, Yu M, Li X, et al. Retinoic acid inhibits the angiogenesis of human embryonic stem cell-derived endothelial cells by activating FBP1-mediated gluconeogenesis. *Stem Cell Res Ther*. 2022;13:239. doi:10.1186/s13287-022-02908-x
52. Hu J, Wang J, Li C, Shang Y. Fructose-1,6-bisphosphatase aggravates oxidative stress-induced apoptosis in asthma by suppressing the Nrf2 pathway. *J Cell Mol Med*. 2021;25:5001–5014. doi:10.1111/jcmm.16439
53. Ahmad F, Leake DS. Lysosomal oxidation of LDL alters lysosomal pH, induces senescence, and increases secretion of pro-inflammatory cytokines in human macrophages. *J Lipid Res*. 2019;60:98–110. doi:10.1194/jlr.M088245

54. Broeders W, Bekkering S, El Messaoudi S, Joosten LAB, van Royen N, Riksen NP. Innate immune cells in the pathophysiology of calcific aortic valve disease: lessons to be learned from atherosclerotic cardiovascular disease? *Basic Res Cardiol*. 2022;117:28. doi:10.1007/s00395-022-00935-6
55. Farkhondeh T, Samarghandian S, Bafandeh F. The cardiovascular protective effects of chrysin: a narrative review on experimental researches. *Cardiovasc Hematol Agents Med Chem*. 2019;17:17–27. doi:10.2174/1871525717666190114145137
56. Meng Z, Wang M, Xing J, Liu Y, Li H. Myricetin ameliorates atherosclerosis in the low-density-lipoprotein receptor knockout mice by suppression of cholesterol accumulation in macrophage foam cells. *Nutr Metab*. 2019;16:25. doi:10.1186/s12986-019-0354-7
57. Kong L, Luo C, Li X, Zhou Y, He H. The anti-inflammatory effect of kaempferol on early atherosclerosis in high cholesterol fed rabbits. *Lipids Health Dis*. 2013;12:115. doi:10.1186/1476-511X-12-115
58. Thomas SD, Jha NK, Jha SK, Sadek B, Ojha S. Pharmacological and molecular insight on the cardioprotective role of apigenin. *Nutrients*. 2023;15:385. doi:10.3390/nu15020385